Design and Analysis of a Sun Sensor for Planetary Rover Absolute Heading Detection

Ashitey Trebi-Ollennu, Terry Huntsberger, Yang Cheng, E. T. Baumgartner, Brett Kennedy, and Paul Schenker

***Abstract*—This paper describes a new sun sensor for absolute heading detection developed for the Field Integrated, Design and Operations (FIDO) rover. The FIDO rover is an advanced technology rover that is a terrestrial prototype of the rovers NASA/Jet Propulsion Laboratory (JPL) plans to send to Mars in 2003. Our goal was to develop a sun sensor that fills the current cost/performance gap, uses the power of subpixel interpolation, makes use of current hardware on the rover, and demands very little computational overhead. The need for a sun sensor on planetary rovers lies in the fact that current means of estimating the heading of planetary rovers involves integration of noisy rotational-speed measurements. This noise causes error to accumulate and grow rapidly. Moreover, the heading error affects the estimate of the x and y position of the rover. More importantly, incremental odometry heading estimation is only reliable over relatively short distances. There is an urgent need to develop a new heading-detection sensor for long traverses [for example, 100 m per Sol (Martian Day)], as requested for future Mars mission. Results of a recent FIDO field trial at Black Rock Summit in Central Nevada and several operations readiness tests at the JPL MarsYard using the sun sensor have demonstrated threefold to fourfold improvement in the heading estimation of the rover compared to incremental odometry.**

***Index Terms*—Celestial navigation, heading detection, planetary rovers, rover localization, state estimation.**

I. Introduction

The successful use of celestial navigation sensors (e.g., sun sensors and star trackers) by spacecraft and marine vehicles have attracted great interest in their use by planetary robotists because there are currently no immediate plans by NASA to install Global Positioning Systems (GPS) for other planets. Magnetic heading detection devices are not viable because most of the planets in our solar system have negligible magnetic fields. Absolute heading detection for planetary rovers remains the most significant of the navigation parameters in terms of its influence on accumulated dead-reckoning errors. For example, in an odometry-based positioning rover, any small orientation error will cause a constant growth in the lateral position error. Therefore, sensors that can provide a measure of absolute heading are of extreme importance in developing long-range navigation algorithms for future autonomous planetary rovers.

Of all the celestial bodies, the sun is the most attractive for navigation. In the past twenty years, a sun sensor has been used on every satellite launched for both attitude determination and attitude control. Two key factors make the sun the most attractive celestial body for navigation [1]. First, the sun is sufficiently bright; it is, therefore, easy to detect without the need to discriminate among other celestial sources. Second, the sun's angular radius is nearly orbit-independent and sufficiently small (0.267 degrees at 1 AU) that it suffices to model it as a point source.

In 1998, Doraiswami [2] developed a sun sensor for planetary rovers consisting of a lateral-effects sensor located at the focal plane of a system of lenses that capture the incoming sunlight. The lateral-effects sensor functions as a two-dimensional (2-D) photodiode that locates the position of the sunlight focused on the detector surface. The Sun sensor outputs four signals corresponding to the distance of the focus light from each of the four corners of the sensor plane. Using a robust Kalman filter estimation scheme, the x- and y-position coordinates of the sunlight in the sensor frame is computed. The redundancy in the measurement is exploited to detect and isolate erroneous sensor measurement. However, the developed sun sensor was never used on a real rover and is computationally expensive for real-time implementation.

Fig. 1. Sun sensor mounted on the FIDO rover.

Volpe [3] reports the use of a sun sensor in long-range mission scenario field trials on Rocky 7, a Mars technology rover prototype at NASA's Jet Propulsion Laboratory (JPL). The sun sensor is very similar to the sun sensor developed by Doraiswami [2] and was developed by Lockheed Martin Astronautics in Denver. The sun sensor integrates overall light input from its field of view and outputs an analog signal proportional to the perceived sun centroid of the image. Although the sun sensor update rate is relatively fast with very little computation, it requires a fairly complex calibration process and is sensitive to stray scattering of light from haze. Any slight miscalibration leads to significant errors in the output.

The goal of the Field Integrated, Design and Operations (FIDO) Rover team was to develop a sun sensor that fills the current cost/performance gap, uses the power of subpixel interpolation, makes use of current hardware on the rover, and demands very little computational overhead. In addition, a great deal of emphasis was placed on robustness to calibration errors and the flexibility to make a transition to a flight rover with very little modification. The resulting sun sensor, which is shown in Fig. 1, consists of a charge-coupled device (CCD) monochrome camera, two neutral-density filters, a wide-angle lens (FOV 120×84 degrees), and housing. Fig. 1 depicts the sun sensor mounted on FIDO. The neutral-density filters are attached to the camera lens so that the Sun can be observed directly. The neutral-density filters reduce incident light to capture only the Sun's disk. The sun sensor camera is modeled as a fish eye camera/lens system with 21 external and internal camera parameters. These parameters are computed in a calibration procedure that describes the mapping between 3-D space and the 2-D image plane [4]. The sun sensor captures images using an onboard frame grabber mounted on the rover computing stack. A detailed design and analysis of the sun sensor can be found in [5].

The sections of this paper that follow are organized as follows: Section II presents a brief description of the FIDO rover. Section III presents a detailed description of the concepts and formulation of the sun sensor algorithm. Section IV presents a detailed error analysis of experimental results from the sun sensor. We particularly focus on

Manuscript received February 7, 2001 revised September 10, 2001. This paper was recommended for publication by Associate Editor D. Kriegman and Editor S. Hutchinson upon evaluation of the reviewers' comments. This work was supported by the National Aeronautics and Space Administration.

The authors are with the National Aeronautics and Space Administration (NASA), Jet Propulsion Laboratory, California Institute of Technology, Pasadena, CA 91109 USA (e-mail: ashitey@jpl.nasa.gov).

Publisher Item Identifier S 1042-296X(01)11166-3.

Fig. 2. FIDO rovers with the mast and instrument arm deployed at Black Rock Summit.

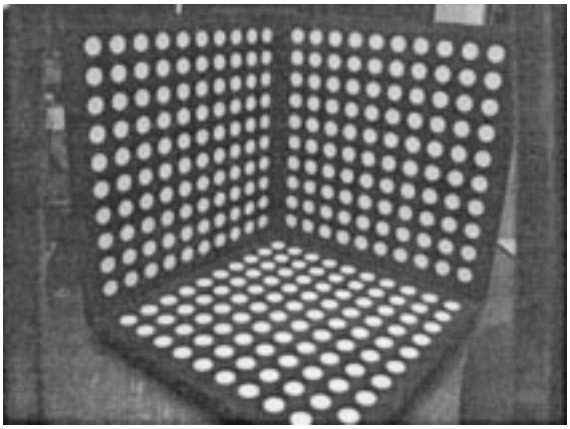

Fig. 3. Picture of the calibration target.

performance in both diffuse and nondiffuse atmospheres, at mid-latitudes, and between mid-morning and mid-afternoon sun elevation, which are the relevant conditions for mission operations on the surface of Mars. This is followed by some experimental studies in Section V. The paper closes with conclusions in Section VI.

II. FIDO Rover

The FIDO rover is an advanced technology rover that is a terrestrial prototype of the rover that NASA/JPL plans to send to Mars in 2003.[1] FIDO's mobility subsystem consists of a six-wheel rocker-bogie suspension system [6] and is capable of traversing over obstacles up to 30 cm in height. FIDO is equipped with an analog of the science payload that the flight rover will carry [7].

FIDO has a 4-degrees-of-freedom (DOF) mast that extends to 1.94 m when deployed (as shown in Fig. 2). When the vehicle is moving, the mast is stowed on the rover deck. The mast-head houses a stereo PanCam (panorama camera), a stereo NavCam (navigation camera), and an Infrared Point Spectrometer (IPS). The PanCam has a three-band near-infrared imaging system capable of surveying the terrain in stereo with high spatial resolution for scientific purposes. The NavCam is a low spatial-resolution, monochrome, wide field-of-view stereo imaging system used for traverse planning. The IPS is bore sighted with NavCam and PanCam and is used to acquire spectral radiance information in either a point or raster mode. In addition to the mast, FIDO has a 4-DOF Instrument Arm, a Mini-Corer, and BellyCam (a stereo camera) mounted on the underside or "belly" of the front of the rover. A color microscopic imager is mounted on the end-effector of the Instrument Arm. The Mini-Corer can be used to acquire sample cores from rocks of 0.5-cm diameter and up to 1.7 cm long. FIDO has two other sets of stereo cameras, called the Front HazCam and the Rear HazCam. The HazCams are used to provide range data for autonomous hazard avoidance algorithm for obstacle detection during rover traverses. The front HazCam is also utilized to choose science targets for *in situ* instruments mounted on the Instrument Arm.

The rover-computing platform is a PC/104 266Mhz, Pentium-class CPU with a VxWorks 5.4 real-time operating system. FIDO uses a three-layer software architecture: the lowest layer is the device driver layer (DDL), the middle layer is the device layer (DL), and the top layer is the application layer (APL). The DDL handles all hardware dependencies (e.g., DIO, Counters, A/D drivers). The DDL provides the means for abstracting the higher-level software in the APL from the hardware dependencies. The DDL is responsible for all motion-control functions, vision processing, instrument interfaces, forward and inverse kinematics for the Mast and Instrument Arm, etc. The APL contains all rover sequences, instrument sequences, Sun sensor algorithm, and hazard-detection and path-planning software. The software on FIDO is written in ANSI-C.

FIDO has been used to simulate operational concepts for future Mars surface exploration missions. Recent blind field tests (May 2000) in Black Rock Summit in Nevada helped shape the rover mission specifications outlined by NASA for 2003 mission to Mars. During field trials [9], operations are directed from JPL by the actual Mars mission flight science team members and distributed collaborative users all over the world via the Internet. The Web Interface for Telescience (WITS) and the Multi-Mission Encrypted Communication System (MECS) [10] are used for sequence planning and generation, and command and data product recovery. Rover localization information is accomplished using a sensor fusion framework combining wheel odometry with a sun sensor and inertia navigation unit (INU) sensors to provide an integrated state estimate for the rover position and orientation relative to a fixed site reference frame. The state estimation algorithm used is based on an extended Kalman filter [8], [19].

III. Sun Sensor

This section outlines the detailed concepts and formulation of the sun sensor algorithm.

A. Camera Model

To correctly predict 3-D rays of objects from their respective camera 2-D images, a geometric calibration of the camera is required. Geometric calibration of a camera entails correctly modeling the optical path of the camera. A typical approach to geometric calibration of a camera is to take an image of a precisely known target and use the geometric properties of the target to determine the lens and camera parameters. Fig. 3 depicts a camera calibration target used at JPL. The camera target has three 1-m^2 components that are made from aluminum and anodized to have a dull, matte black color. As shown in Fig. 3, each face of the calibration targets has a 10×10 grid of 5-cm-diameter white circles stamped on it. The three faces are assembled to form the "inside corner" of a cube. The camera calibration process relies on the accurate detection of the centroid of the white dots found on each face of the calibration target relative to the known physical location of the centroid relative to the calibration target reference coordinate frame.

The basic camera model used at JPL's Planetary Robotics Laboratory is comprised of six 3-vector parameters — $\mathbf{c}$, $\mathbf{a}$, $\mathbf{h}$, $\mathbf{v}$, $\mathbf{o}$, and $\mathbf{r}$ (CAHVOR) — expressed in an object-coordinate frame [11]. The vector $\mathbf{c}$ defines the position of the perspective center of the camera lens (focal center). The vector $\mathbf{a}$ is a unit vector pointing outwards from

[1]Available. [Online.] http://fido.jpl.nasa.gov

the camera and *parallel to a normal* from the exit pupil pointing to the image sensor plane. The vectors $\mathbf{h}$ and $\mathbf{v}$ are vectors in the sensor plane and are perpendicular to the x and y image axes, respectively ($\mathbf{h}$ and $\mathbf{v}$ are not necessarily orthogonal). The vector $\mathbf{o}$ is a unit vector used to represent the optical axis. The radial distortion polynomial $\mathbf{r}$ of the camera lens system is defined relative to $\mathbf{o}$.

However, the CAHVOR lens camera model cannot adequately model the sun sensor camera because a wide-field-of-view (FOV) (120 degrees) lens is being used. Therefore, an extension of the CAHVOR camera model, known locally as CAHVORE, was used. The major difference between CAHVOR and CAHVORE is that the CAHVORE assumes the entering ray is projected at $r = f\sum_i c_i\rho^i$ instead of $r = f\tan\rho$, where ρ is the angle between the entering ray and the optical axis, f is the focal length of the lens, i runs from 1 to 3, and r is the offset from the center of the image plane [4].

The camera calibration algorithm uses nonlinear least squares adjustments to operate on a calibration target image. The camera model parameters are adjusted to minimize the sum of the squares of the residuals in the image plane. During calibration of the sun sensor camera, the camera was rigidly mounted in front of the calibration target shown in Fig. 3. The camera was aimed directly at the point where all three faces of the target meet. The camera position was iteratively adjusted until the two vertical faces of the target covered most of the image. The image was run through the camera-calibration algorithm described above to generate a 21-parameter camera model. The rms error for the camera model was 0.25 pixels. This subpixel value indicates a good fit and minimizes the effect of the camera model on sun sensor measurements.

B. Feature Extraction

The centroid of the sun in the image is the main feature needed for determination of the rover heading. The neutral density filters in the sun sensor assembly filter out the majority of the low-level light. Centroid extraction follows a three-step process: thresholding, artifact removal, and center of mass/circularity determination. The thresholding operation is based on a fixed threshold that has been experimentally determined using a standard sun sensor assembly. Artifact removal is performed using mathematical morphology operations on the thresholded image similar to those done in [18]. Finally, the first- and second-order shape moments are extracted from the thresholded image to determine the centroid (center of mass) and the circularity.

The neutral density filters reduce incident light to capture only the sun disk. However, the filters may also capture reflections of the sun onto clouds and secondary reflections from the surface of the lens assembly. Both of these types of artifacts can potentially influence the accuracy of the centroid determination. An example of a raw sun sensor image is shown in Fig. 4. This image has all three types of artifacts and also includes blooming of the CCD sensor from saturation. We have defined a confidence measure based on the relative percentage of blooming and cloud cover or haze in the image. Such a measure is vital for sun sensor use on Mars, where there may be extensive haze due to global dust storms and/or localized dust devils. The confidence measure is used to decide whether to include the sun sensor reading during the Extended Kalman Filter update of the rover heading. This confidence measure is given by

$$\mathrm{conf\_measure} = \frac{1.0 - \mathrm{conf\_count}}{\mathrm{Size} - \mathrm{count}} \tag{1}$$

where Size is the total image size in pixels, count is the total number of pixels above the threshold for sun pixel candidates (gray scale value of 220), and $\mathrm{conf\_count}$ is the total number of pixels that have a threshold greater than an experimentally determined background level (gray scale value of 70) and less than the Sun pixel threshold. This confidence measure will be 1.0 if all pixels in the image are sun-pixel candidates. It does not include the spatial effect of multiple regions that are above the sun-pixel threshold. The confidence measure for the sun image in Fig. 4 is 0.896.

Fig. 4. Original sun sensor image.

Fig. 5. Image after threshold operation.

Fig. 6. Image after application of open operation.

The output of the thresholding operation on the image in Fig. 4 is shown in Fig. 5, where all pixels below the threshold have been set to zero. The blooming has been eliminated. In addition, most of the clouds with the exception of those closest to the sun have also been suppressed. Small secondary reflections appear as isolated point-like structures throughout the image. The mathematical morphology open operation [12] is used to further suppress the smaller cloud and secondary reflection artifacts.

This operation has the effect of removing any objects that are less than the neighborhood size and is usually used for noise removal. We use the operator to remove objects that would not be good sun candidates due to size. The output of the application of the operator to the thresholded image of Fig. 5 is shown in Fig. 6, where the smaller artifacts caused by clouds and secondary reflections have been eliminated. All that remains are two regions: the sun and the closest cloud-patch, which has been reduced to a compact shape (see Fig. 6).

The primary difference between the sun region and the cloud artifact is the circularity of the sun. In the event that there is more than one region (as seen in Fig. 6), a region-growing process must be run first, followed by the first-order shape-moment extraction for centroid determination [13]. This will give more than one centroid; and the second-order shape moments μ_{11}, μ_{02}, and μ_{20} as defined in [13] are used to evaluate the circularity and standard deviation of each region. These measures are position independent. A perfectly circular region

is characterized by $\mu_{11} = 0$. We use the relative magnitude to determine the circularity of a region. For the two regions in Fig. 6, the value of $\mu_{11} = -9710$, $\sigma_x = 11.39$, and $\sigma_y = 12.46$ for the sun and $\mu_{11} = 37\,985$, $\sigma_x = 9.43$, and $\sigma_y = 9.20$ for the cloud artifact. A $\mu_{11} = -9710$ is closer to zero than that of $\mu_{11} = 37985$, meaning the first object is the sun.

C. Sun Azimuth and Elevation Computation Using a Sun Sensor

Given the 2-D Sun centroid from the threshold Sun image, a 3-D unit ray vector $s = [\, s_x \quad s_y \quad s_z \,]^T$ is computed from the sensor to the sun using the CAVHORE model. The sun's azimuth (α_s) and elevation (ζ_s) in the sensor frame are related to the components of the 3-D unit ray vector **S** as follows:

$$CA = \cos\zeta_s, OA = \sin\zeta_s, BA = \sin\alpha_s \sin\zeta_s, \text{ and } OB = \cos\alpha_s \sin\zeta_s. \quad (2)$$

From (2), $s = [\, s_x \quad s_y \quad s_z \,]^T$ is defined as

$$\begin{bmatrix} s_x \\ s_y \\ s_z \end{bmatrix} = \begin{bmatrix} \cos\alpha_s \sin\zeta_s \\ \cos\zeta_s \\ \sin\alpha_s \sin\zeta_s \end{bmatrix}. \quad (3)$$

The 3-D unit ray vector **s** is transformed to the rover frame as $s_R = [\, s_{Rx} \quad s_{Ry} \quad s_{Rz} \,]^T$, where the components of S_R are defined as follows:

$$\begin{bmatrix} s_{Rx} \\ s_{Ry} \\ s_{Rz} \end{bmatrix} = \begin{bmatrix} 0 & 0 & 1 \\ -1 & 0 & 0 \\ 0 & -1 & 0 \end{bmatrix} \begin{bmatrix} s_x \\ s_y \\ s_z \end{bmatrix}. \quad (4)$$

The transformation matrix from the sensor frame to rover frame can be derived from Fig. 7 by inspection. From (3) and (4), the sun's azimuth and elevation can be computed in the sensor and rover frame, respectively. However, we are interested in computing the heading of the rover in the site fixed gravity-down reference frame. The 3-D unit ray s_R is transformed to the site-fixed gravity-down reference frame. The site-fixed gravity-down reference frame is depicted in Fig. 7. The x_{site} axis is aligned to True North, the y_{site} axis is aligned to East, and the z_{site} axis points downward parallel to gravity. Let us assume that the rover coordinate frame is aligned with the site-fixed gravity-down reference coordinate frame. The attitude of the rover changes as it drives over undulating natural terrain. On FIDO, the rover's attitude is obtained from an onboard inertial navigation sensor. The inertial measurement sensor has three rate gyros and three accelerometers for measuring rover angular rates and accelerations, respectively. The accelerometers are used to estimate the rover's pitch and roll.

To derive the rotational matrix that will transform the rover from any given attitude to the level coordinate frame, we must assume that the rover is stationary and the rover coordinate frame is coincident with the level frame (i.e., a site-fixed reference frame). If the rover is pitched θ about the rover y_R axis and rolled ϕ about the rover x_R axis, the rover's position vector in the rover frame can be expressed as follows [14]. The rotation matrix for transforming points in the site-fixed, reference-coordinate frame to the rover frame is determined as

$$T = \begin{bmatrix} \cos\theta & 0 & -\sin\theta \\ \sin\phi\sin\theta & \cos\phi & \sin\phi\cos\theta \\ \cos\phi\sin\theta & -\sin\phi & \cos\phi\cos\theta \end{bmatrix}. \quad (5)$$

During initial alignment, the rover is assumed stationary. The velocities and accelerations of the rover can be considered to be zero (except for gravity). The rover's acceleration at stand still is $\lambda = [\, 0 \quad 0 \quad g \,]$,

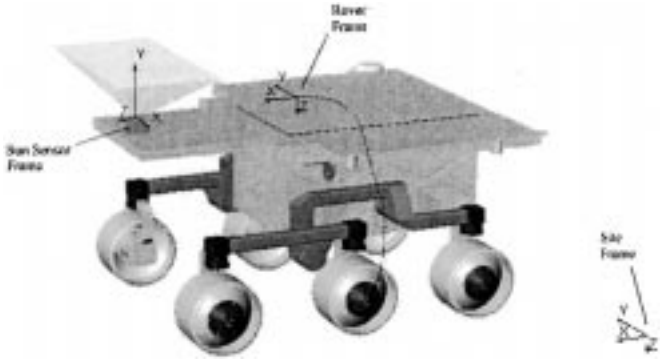

Fig. 7. Rover, sun sensor, and site frames with illustrative pyramid for sunsensor FOV.

where g is gravity. The rover's stationary unit vector acceleration (λ/g) in the rover frame can be expressed as follows using (5), [15] and [16]:

$$\begin{bmatrix} a_{Rx} \\ a_{Ry} \\ a_{Rz} \end{bmatrix} = \begin{bmatrix} -\sin\theta \\ \sin\phi\cos\theta \\ \cos\phi\cos\theta \end{bmatrix}. \quad (6)$$

From (6), the component of the rotational matrix (5) can be determined in terms of the rover's acceleration in rover frame as follows:

$$\sin\theta = -a_{Rx}. \quad (7)$$

From trigonometry identities, and (7),

$$\cos\theta = \sqrt{1 - (a_{Rx})^2} \equiv \nu. \quad (8)$$

From (6), (7), and (8),

$$\sin\phi = \frac{a_{Ry}}{\nu} \; and \; \cos\phi = \frac{a_{Rz}}{\nu}. \quad (9)$$

In the case of rotating the 3-D unit ray $\mathbf{s}_R$ to the site-fixed gravity-down reference frame, the inverse of the rotational matrix in (5) is required. However, the rotational matrix of (5) is a special orthogonal matrix where $T^{-1} = T^T$. The rotational matrix for rotating from the rover frame to the site-fixed reference frame is given by

$$G = T^T = \begin{bmatrix} \nu & \frac{-a_{Ry}a_{Rx}}{\nu} & \frac{-a_{Rz}a_{Rx}}{\nu} \\ 0 & \frac{a_{Rz}}{\nu} & \frac{-a_{Ry}}{\nu} \\ a_{Rx} & a_{Ry} & a_{Rz} \end{bmatrix}. \quad (10)$$

The 3-D unit ray $\mathbf{s}_{\text{site}} = [\, s_{sx} \quad s_{sy} \quad s_{sz} \,]^T$ is obtained as follows:

$$\mathbf{s}_{\text{site}} = \mathbf{G}\mathbf{s}_R. \quad (11)$$

The azimuth α_{site} and elevation ζ_{site} of the Sun in the site-fixed gravity-down reference frame can be computed as follows:

$$\alpha_{\text{site}} = a\tan 2(s_{sx}, s_{sy}) \text{ and } \zeta_{\text{site}} = \sin^{-1}(s_{sz}). \quad (12)$$

1) Sun Azimuth and Elevation Computation Using Ephemeris Data: For a given universal time (UT), the astronomical position of the sun is fixed and can be obtained from the Astronomical Almanac. A real-time algorithm was developed from a shareware program obtained from the Astronomy and Numerical Software web site [17]. The program was significantly modified to simplify it and make it com-

putational efficient for real-time implementation. The algorithm uses solar ephemeris data and solves Kepler's equation and the equation of time to determine the position of the sun (azimuth and elevation) for a given geodetic longitude, latitude, and UT. UT is obtained from the rover computer clock and corrected to the nearest second. From UT, Julian Day is computed and transformed to Ephemeris Time.

2) Rover Heading Computation: Using the sun position (azimuth and elevation) from the sun sensor and solar ephemeris data, the rover's absolute heading with respect to True North is computed. For a given longitude, latitude, altitude, and UT, the astronomical and sun sensor position of the sun are determined as described above. If the astronomical position of the sun is determined by azimuth α_{astron} and elevation ζ_{astron} and the Sun sensor position of the Sun is determined by azimuth α_{site} and elevation ζ_{site} (both are measured in degrees with respect to True North), the rover's heading with respect to True North (in degrees) is computed as follows:

$$\begin{aligned} &If\,(\alpha_{\text{astron}} > \alpha_{\text{site}}) \\ &Rover\_Heading = \alpha_{\text{astron}} - \alpha_{\text{site}} + \delta_{\text{bias}} \\ &\qquad else \\ &Rover\_Heading = \alpha_{\text{site}} - \alpha_{\text{astron}} + \delta_{\text{bias}} \end{aligned} \tag{13}$$

where δ_{bias} is a systematic bias term that can be determined from experimentation. The bias term can be attributed to several factors, including: elevation of the sun, 2-D centroid location in the sensor image plane, mechanical misalignment of the sensor with the rover's x axis, and the CCD camera misalignment in the sun sensor housing. The sun sensor algorithm described above was implemented in ANSI-C in the application layer of the FIDO software architecture.

IV. Error Analysis

In this section, we present an analysis of the impact of parametric uncertainty on the performance of the sun sensor. In general, parametric models obtained using physical system modeling (e.g., a camera model), parameter estimation (e.g., the sun's centroid estimation in image plane), or a combination of both will be subject to uncertainty in some, if not all of the parameters. In this analysis, we will characterize (i.e., quantify) and assess the dominant parametric uncertainties and their effect on the performance of the sun sensor. Methods for analyzing uncertainties overall assume unstructured uncertainty, which means only information concerning the upper bound on the magnitude of the perturbation measured is employed.

In general, care is usually required in selecting the dominant and distinct elements, or states, of a system to be used to formulate parameter uncertainty. This approach relies heavily upon the designer's knowledge and experience of what is technically feasible and practical. In the case of the sun sensor, there are several candidates: the camera model, an estimate of 2-D sun image centroid, sun elevation, and the attitude (roll and pitch) of the rover. Uncertainties in the camera model parameters are beyond the scope of this paper. The interested reader is referred to [4]. Sensitivity analysis of the sun sensor will focus on perturbation models for sun centroid, sun elevation, and rover attitude.

A. Impact of Sun Centroid Uncertainty on Sun Sensor Output

Section III-B presented the procedure for the estimation of a sun image 2-D centroid and corresponding confidence. The complement of the confidence measure is, in effect, the degree of uncertainty in the 2-D centroid estimate.

1) 2-D Centroid Position Dependent Error: To determine the error introduced by uncertainties in the estimated position of the 2-D centroid, the geometry of the imaging system comes into play. The error for determination of the angle φ is given by

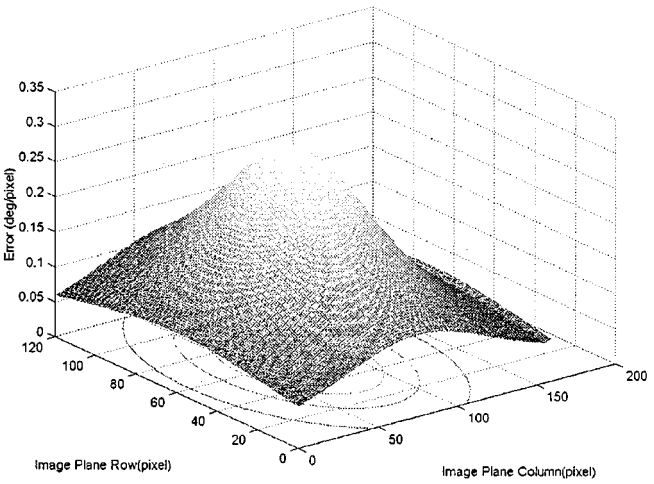

Fig. 8. 3-D plot of 2-D centroid position relative error/pixel plot inimage plane (120×160 pixels.

$$\delta\varphi = \frac{f}{(f^2 + x^2)} \tag{14}$$

where f is the focal length of the lens and x is the offset from the center of the image plane. The relative error/pixel decreases quadratically with distance from center of the image plane. The focal length for the lens is 2.5 mm; the width of the image plane is 8.4 mm. This geometry gives an error of 0.3 degrees/pixel in the center of the image, as shown in Fig. 8. The contour plot in Fig. 8 illustrates that the error has decreased by 16% to 0.25 degrees/pixel at 20 pixels away from the center of the image.

Another error source is the heading error in the estimation of centroid of the Sun. This heading uncertainty ξ can be calculated as $\xi = s/r$, where s is the uncertainty in the centroid location and r is the distance from the center of the image. This measure is undefined if it coincides with the terrain surface normal; however, at 1 pixel away the measure is equal to 57.3° for a centroid uncertainty of 1 pixel. This is by far the main source of error in heading determination. The above analysis helped determined a cut-off region for centroid location in the image plane. A centroid located within a 20-pixel radius from the terrain surface normal in the image is discarded. In the cut-off region, an uncertainty of 1 pixel in the centroid will result in at least a 2 degree heading error, which is not acceptable.

2) Impact of Rover Attitude Uncertainty on Sun Sensor Output: As stated earlier, the FIDO rover is equipped with an onboard IMU to provide attitude information (roll and pitch) and attitude-rate information (roll rate, pitch rate, and heading rate). Uncertainty in the rover attitude may be a result of sensor imperfection, computational errors, and alignment errors. In addition, during rover traverse, the onboard IMU may be subjected to nonlinear vibration; since such motion arises as a result of rover wheels/terrain interaction.

Let Δ_a be a block-diagonal matrix structure containing norm-bounded perturbations of the rover attitude roll and pitch, as follows:

$$\Delta_a = \begin{bmatrix} \delta_\phi & 0 \\ 0 & \delta_\theta \end{bmatrix} \text{and} \|\delta_\phi\| \le \vartheta_\phi \text{and} \|\delta_\theta\| \le \vartheta_\theta \tag{15}$$

where δ_ϕ and δ_θ represents the multiplicative perturbations and ϑ_ϕ and ϑ_θ represent norm-bounds in the roll and pitch attitude of the rover,

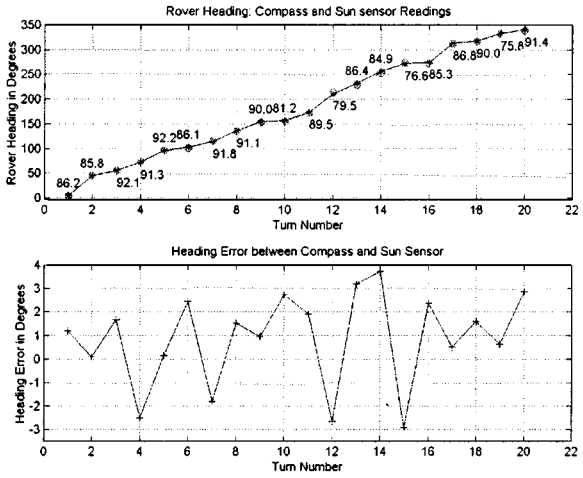

Fig. 9. A plot of rover heading from compass ($*$) and sun sensor ($\circ$).

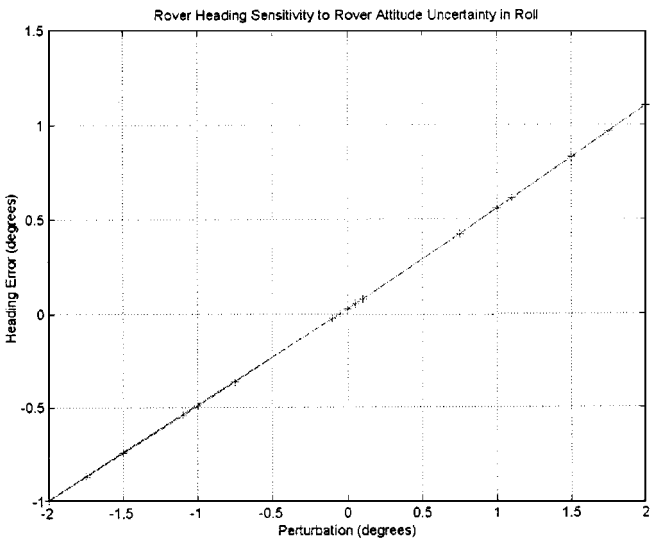

Fig. 10. A plot of rover roll angle uncertainty impact on sun sensor rover heading detection.

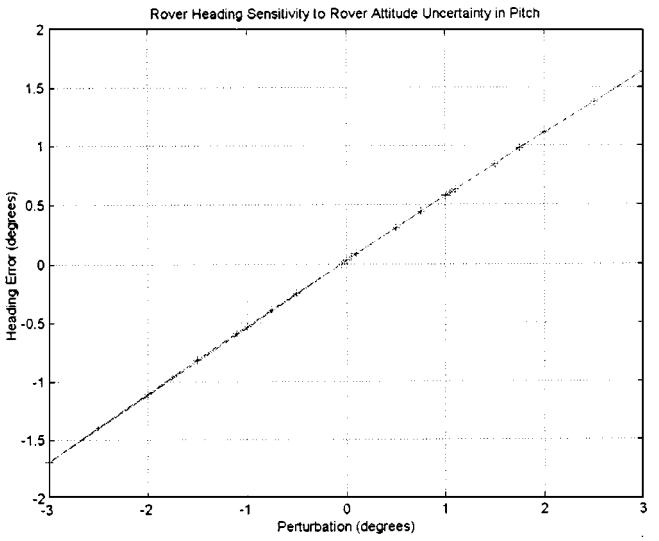

Fig. 11. A plot of rover pitch uncertainty impact on sun sensor rover heading detection.

respectively. If the attitude of the rover is $A_r = [\phi, \theta]^T$, a multiplicative perturbation model for the rover attitude can be expressed as follows:

$$\delta_\phi \leq \vartheta_\phi \phi \text{ and } \delta_\theta \leq \vartheta_\theta \theta. \tag{16}$$

Equation (15) represents a relative measure of the uncertainty in terms of the nominal value. Using (16) the rover attitude can now be expressed as follows:

$$\mathbf{A}_r \leq \begin{bmatrix} \phi\,(1+\vartheta_\phi) \\ \theta\,(1+\vartheta_\theta) \end{bmatrix}. \tag{17}$$

Using (17), a complete sensitivity analysis of rover attitude uncertainties and its impact on the sun sensor output can be investigated (refer to Section V for experimental results).

3) Impact of the Sun's Elevation on Sun Sensor Output: The earth travels around the sun in a circular orbit, with a different tilt angle from the sun at different times of the year. This causes seasonal changes on earth. For example, the summer sun is at a higher elevation in the sky than the winter sun. In addition, in the early morning or late afternoon (sunrise or sunset), the sun is low in the sky in both the summer and winter. Typically, the sun is at an angle that is most nearly vertical near solar noon (refer to Section V for experimental results).

V. Experimental Studies

An experiment was conducted with FIDO placed on a flat surface and incrementally turned in place at increments of about 20 degrees.

Fig. 9 depicts FIDO rover headings recorded by a magnetic compass and the sun sensor from the experiment. The sun sensor confidence for each reading is also indicated on the plot. In addition, Fig. 9 depicts the error between the compass and the sun sensor readings, which is within ± 3 degrees. The accuracy of the magnetic compass used is ± 1 degree. Similar results were obtained with the sun sensor in the field trials (May 2000, 2001) and the operation readiness test. The errors can be attributed to several factors, including mechanical alignment errors of the sun sensor, rover attitude errors, and atmospheric conditions (cloud cover). The sections that follow describe the sensitivity analysis conducted to determine the dominant factors or parameter uncertainties that adversely affect the output of the sun sensor.

In order to test the sensitivity of the sun sensor algorithm to rover attitude, an experiment was setup on a cloudless day at JPL in Pasadena, California. The rover was positioned such that the sun was within the FOV of the sun sensor. The rover's attitude was as follows: roll $= -0.906\,476$ degrees and pitch $= -15.446\,365$ degrees. Using the sun sensor, an image of the sun was captured at 13 hours, 57 minutes, 27 seconds on 31 October 2000. The 2-D centroid of the sun image was estimated to be $p_{\text{row}} = 181.197$ (pixels) and $p_{\text{col}} = 42.2379$ (pixels), with a confidence of 98.87%. Rover heading with respect to True North was determined to be 154.0154 (degrees). For the sensitivity analysis that follows, the set of values for the centroid given above were assumed to be the nominal values (99% confidence is close to ideal). To investigate the effect of rover roll uncertainty on the output of the sun sensor, the norm-bound perturbations of rover roll and pitch were set as follows: $\vartheta_\phi = \pm 2.21$ and $\vartheta_\theta = 0.0$. Using (17) and these values, the sun sensor algorithm was run offline. The result is depicted in Fig. 10. In the case of rover pitch uncertainty, the perturbation norm-bounds were set as follows: $\vartheta_\phi = 0.0$ and $\vartheta_\theta = \pm 0.13$. The results are shown in Fig. 11.

From Figs. 10 and 11, we observe that rover attitude uncertainty (in both roll and pitch) less than $\pm 2^\circ$ have no significant effect on the sun sensor output. However, uncertainties greater than $\pm 2^\circ$ can result in heading errors greater than $\pm 1^\circ$. In addition, we observe that the attitude uncertainty and its effect on heading error is a linear relation with a gradient of 0.5° rover heading error per degree error in rover

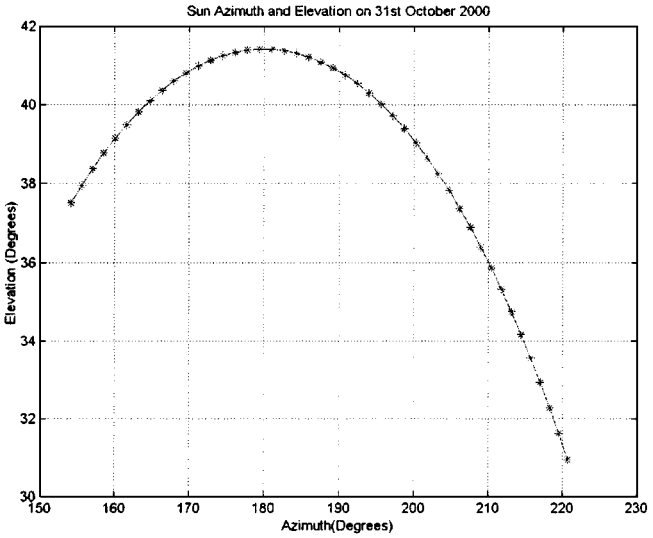

Fig. 12. From a fixed location on earth (JPL), the sun's position from 10 am to 2 pm on 31st October, 2000, using ephemeris data and equation of time.

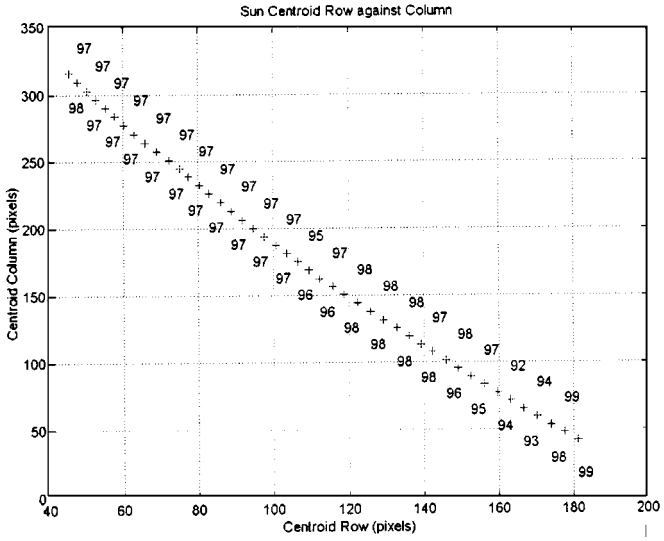

Fig. 13. Two-dimensional location of sun in images taken on 31st October, 2000, from 10 am to 2pm.

attitude. This suggests that if the rover attitude sensor is fairly robust, with a resolution of less than a degree, the rover attitude will have no significant effect on the sun sensor output.

Further experiments demonstrated that a gyroscopic bias of 0.01 degree/s would be more than suitable for the sun sensor because the operation times for planetary rovers are typically on the order of a few hours.

In the next experiment, we investigated the sensitivity of the sun sensor output with respect to the sun's elevation over a 4-h period (a typical operational period for a planetary rover). The sun sensor FOV is rather restrictive; hence, the sun is within the sensor FOV from about 10:00 am to 2:00 pm in the winter. This is only achieved after judicious positioning of the rover. On 31 October 2000 at 10:12 am, the rover was positioned with attitude, roll $= -0.906\,476$ degrees and pitch $= -15.446\,365$ degrees such that the sun was within the view of the sun sensor. At 5-min intervals, a sun sensor reading of the rover heading was collected until 1:57 pm (approximately a 4-h period). The day was cloudless, effectively eliminating or reducing the influence of atmospheric uncertainties as major factor in the sun sensor output. The average confidence measure for the sun images was 97%, confirming a cloudless day.

Fig. 12 depicts a plot of the sun's azimuth against elevation for the duration of the experiment. The sun's elevation and azimuth were obtained from ephemeris data and equation of time. Fig. 13 depicts the trace of the 2-D location (centroid) of the sun in images captured for the duration of the experiment. In contrast to Fig. 12, 13 is almost a straight line, the reason being that the sun is at infinity with respect to the sun sensor. Consequently, the radius of curvature is infinity; hence, the straight line. Also, the 2-D sun centroid is moving across the image plane from left to right (see Fig. 13).

Fig. 14 shows the rover heading error against time, which can be interpreted as a plot of rover heading error against sun elevation. In Fig. 14, the heading error follows a quadratic profile with respect to the sun's elevation. There are two main reasons for this trend. The first reason is that the sun is moving across the image plane from a region of least error/pixel through the region with the worst error/pixel to a region of least error/pixel (see Fig. 8) as discussed in Section IV-A1. The second reason is that, as the sun elevation rises, the sun captured in the image is relatively large and noncircular (as compared to low elevation sun images). Similarly, at extremely low elevations, the sun disk is very small and noncircular. The noncircularity and enlarged or

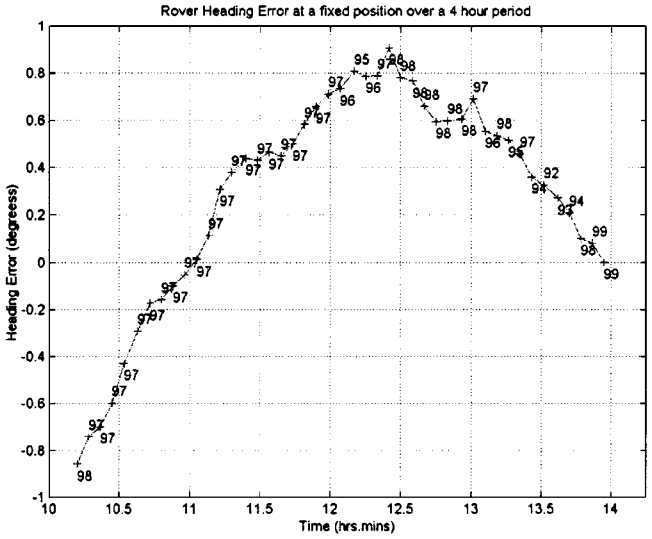

Fig. 14. A plot of rover heading error and corresponding confidence over a four-hour period at a fixed location and cloudless day, 31st October 2000.

reduced image of the sun introduces significant uncertainty in the 2-D sun centroid estimate, leading to relatively large errors at sunrise, solar noon, and sunset. In Fig. 14, the sunrise period corresponds to 10:00 am to 10:30 am; the solar noon period corresponds to 11:45 am to 12:30 pm. Another source of error is the parametric uncertainty in the camera model with respect to the radial distortion of the wide FOV lens. The maximum heading error that occurs about noon is less than a degree. It is safe to conclude that the elevation of the Sun has no significantly impact on the output of the sun sensor. The results obtained from the experiments would be used to formulate a new bias term in (13) to account for elevation of the sun and the location of the 2-D sun centroid in the image plane to further reduce the heading error.

Figs. 15 and 16 depict the results of the experiment described above that was conducted a day earlier (30 October 2000) on a very cloudy day. These results are presented here to demonstrate the robustness of the sun sensor to certain atmospheric conditions (e.g., clouds) and some limitations of the current sun algorithm. Fig. 15 depicts the trace of the 2-D location (centroid) of the sun for the duration of the experiment.

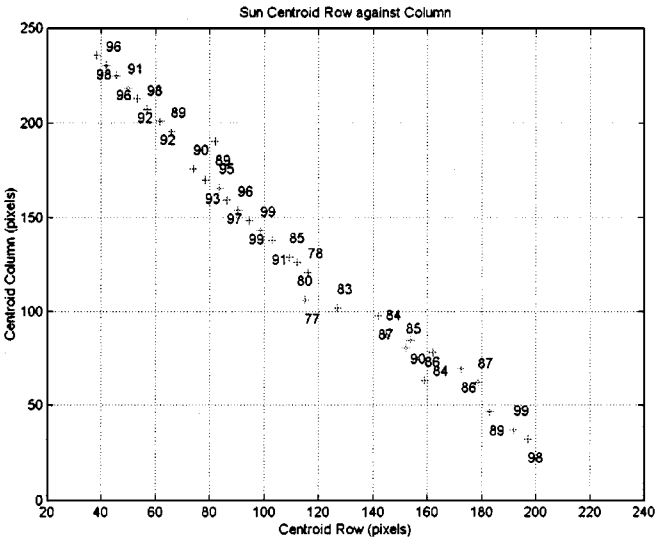

Fig. 15. 2-D location and confidence of sun in images taken on the 30th October 2000 from 10:30 am to 1:40 pm.

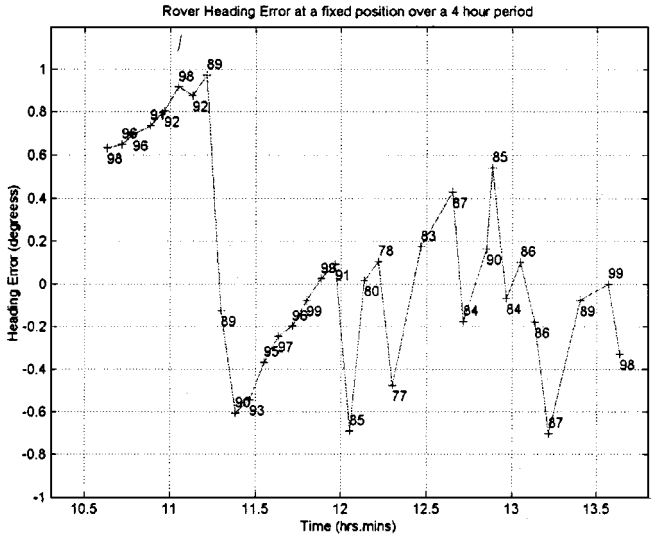

Fig. 16. A plot of rover heading error and confidence over a three-hour period at a fixed location, 30 October 2000.

Fig. 17. Sun image at 11:43 am, 30 October 2000, confidence 98.55%.

The average sun image confidence for the experiment was 82%. Comparing Figs. 16 to Fig. 14 we observe significant point scatter (the effect of cloud cover). Nevertheless, the point scatter of 2-D sun location in Fig. 15 can still be approximated with a straight line.

This demonstrates the robustness of the 2-D sun image centroid determination to atmospheric haze. Fig. 16 further demonstrates the robustness of the sun sensor algorithm; under varying cloud cover, the heading errors are still within 1 degree (although there is a great deal more fluctuation in the heading error compared to Fig. 14, as would be expected).

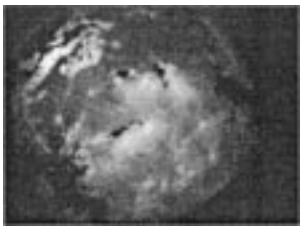

Fig. 18. Sun image at 12:18 pm, 30 October 2000, confidence 76.95%.

Fig. 17 depicts the best sun image for the day with a confidence of about 99% and Fig. 18 depicts the worst sun image for the day with a confidence of about 77%. In Fig. 18, it is virtually impossible to localize the sun; however, the algorithm was able to detect the sun location, resulting in the worst heading error of 0.9 degrees. In addition, the experiment helped determine the cutoff confidence for a good sun image, which is $\geq$ 80%.

VI. Conclusion

In this paper, we have presented extensive analysis, simulation, and experimental results of a new planetary rover sun sensor for rover absolute heading detection. The new sensor can handle the effect of atmospheric conditions (cloud cover), changes in the sun's position, and uncertainty in rover attitude measurements.

A major disadvantage of the current design is the limited field of view of the lens. Research is currently underway to develop a 150×150 FOV sun sensor. Another major challenge is the collection of dust on the sun sensor that would be a key factor for a 90-Sol mission, as planned for 2003. In addition, we are investigating the possible use of the sun sensor to estimate the rover position during a very long traverse (e.g., $\geq$ 10 Km) by employing concepts of solar point or geographic position of a body on a planet and circles of equal latitude. Some tentative results from a previous study along this line can be found in [18].

Acknowledgment

The authors would like to express their sincere appreciation to L. Magnone for his help in the experimental setup during the period of this study. They also owe a special debt of gratitude to T. Ganino for his help with mechanically mounting the sun sensor on the rover and some of the illustrative drawings used in the paper. This research was carried out at the Jet Propulsion Laboratory, California Institute of Technology, under a contract with the National Aeronautics and Space Administration.

References

[1] J. R. Wertz, *Spacecraft Attitude Determination and Control*, J. Wertz, Ed. Norwell, MA: Kluwer, 1995.

[2] R. Doraiswami and R. S. Price, "A Robust Position Estimation Scheme Using Sun Sensor," *IEEE Trans. Instrum. Meas.*, vol. 47, pp. 595–603, 1998.

[3] R. Volpe, "Mars Rover Navigation Results Using Sun Sensor Heading Determination," *Proc. IEEE/RSJ Int. Conf. on Intelligent Robot and Systems*, vol. 1, pp. 460–467, 1999.

[4] Y. Xiong and K. Turkowski, "Creating image-based VR using self-calibrating fisheye lens," *Proc. IEEE Conf. on Computer Vision and Pattern Recongnition*, pp. 237–243, 1997.

[5] A. Trebi-Ollennu, T. Huntsberger, Y. Cheng, E. T. Baumgartner, and B. Kennedy, "Design and Analysis of a Sun Sensor for Planetary Rover Absolute Heading Detection," California Institute of Technology, Jet Propulsion Laboratory, National Aeronautics and Space Administration (NASA), CR-2001–210 800, 2001.

[6] R. Lindemann, L. Reid, and C. Voorhees, "Mobility Sub-System for the Exploration Technology Rover," in *Proc. 33rd Aerospace Mechanisms Symp.*, 1999, pp. 115–130.
[7] E. T. Baumgartner, "In-Situ Exploration of Mars Using Rover Systems," in *Proc. AIAA Space 2000 Conf.*, 2000, AIAA Paper # 2000–5062.
[8] E. T. Baumgartner, H. Aghazarian, A. Trebi-Ollennu, T. L. Huntsberger, and M. S. Garrett, "State Estimation and Vehicle Localization for the FIDO Rover," in *Proc. SPIE Conf. Sensor Fusion and Decentralized Control in Autonomous Robotic Systems III*, vol. 4196, Nov. 2000, pp. 329–336.
[9] R. E. Arvidson, S. Squyres, E. T. Baumgartner, L. Dorsky, and P. Schenker, "Rover Trials for Mars Sample Return Mission Prove Successful," *EOS Trans. Amer. Geophys. Union*, vol. 81, no. 7, pp. 65–72, 2000.
[10] P. G. Backes and J. S. Norris, "Automated Rover Sequence Report Generation," in *Proc. IEEE Aerospace Conf.*, Big Sky, MT, March 2001.
[11] D. B. Gennery, "Camera Calibration Including Lens Distortion," JPL, Pasadena, CA, JPL Tech Report D-8580, 1991.
[12] R. M. Haralick, S. R. Sternberg, and X. Zhuang, "Image analysis using mathematical morphology," *IEEE Trans. PAMI*, vol. 9, no. 4, pp. 532–550, 1987.
[13] M. D. Levine, *Vision in Man and Machine*. New York: McGraw-Hill, 1985.
[14] D. H. Titterton and J. L. Weston, "Strapdown inertial navigation technology," in *IEE Radar, Sonar, Navigation and Avionics Series 5*, E. Bradsell, Ed. London, U.K.: Peter Pergrinus Ltd, 1997, pp. 455–455.
[15] A. Brandt and J. F. Gardner, "Constrained Navigation Algorithms for Strapdown Inertial Navigation Systems with Reduced Set of Sensors," in *Proc. American Control Conf.*, vol. 3, 1998, pp. 1848–1852.
[16] E. Nebot and H. Durrant-Whyte, "Initial calibration and alignment of an inertial navigation," in *Proc. Fourth Annual Conf. on Mechatronics and Machine Vision in Practice*, 1997, pp. 175–180.
[17] S. L. Moshier, "Self-contained ephemeris calculator,", Astronomy and Numerical Software web site (http://people.ne.mediaone.net/moshier/index.html)..
[18] F. Cozman and E. Krotkov, "Robot Localization Using a Computer Vision Sextant," *Proc. IEEE Int. Conf. on Robotics and Automation (ICRA'95)*, pp. 106–111, 1995.
[19] E. T. Baumgartner, H. Aghazarian, and A. Trebi-Ollennu, "Rover Localization Results for the FIDO Rover," in *Sensor Fusion and Decentralized Control in Autonomous Robotic Systems IV*, vol. 4571, SPIE Proc, Newton, MA, 2001.

Formation Constrained Multi-Agent Control

Magnus Egerstedt and Xiaoming Hu

***Abstract*—We propose a model independent coordination strategy for multi-agent formation control. The main theorem states that under a bounded tracking error assumption our method stabilizes the formation error. We illustrate the usefulness of the method by applying it to rigid body constrained motions.**

***Index Terms*—Coordinated control, mobile robots, stability.**

I. Introduction

In the maturing field of mobile robot control, a natural extension to the traditional trajectory tracking problem [4], [7], [9], [15] is that of *coordinated tracking*. In its most general formulation, the problem is to find a coordinated control scheme for multiple robots that make them maintain some given, possibly time-varying, formation at the same time as the robots, viewed as a group, execute a given task. The possible tasks could range from exploration of unknown environments where an increase in numbers could potentially reduce the exploration time, navigation in hostile environments where multiple robots make the system redundant and thus robust [2], to coordinated path following [5]. The latter of these tasks is applicable in manufacturing or construction situations where multiple robots are asked to carry or push objects in a coordinated fashion [11], [13].

In this paper, we focus on a particular type of *path following*, and the idea is to specify a reference path for a given, nonphysical point. Then a multiple agent formation, defined with respect to the real robots as well as to the nonphysical *virtual leader*, should be maintained at the same time as the virtual leader tracks its reference trajectory.

The formation problem for multiple robots has been extensively studied in the literature, and, for instance, in [2] a behavior-based, decentralized control architecture is exploited, where each individual platform makes sure that it is placed appropriately with respect to its neighbors. In [5] and [6], the situation is slightly different and the solution is based on letting one robot take on the role of the leader, meaning that all of the other robots position themselves relative to that robot. Furthermore, in [10], [16], and [18], an extensive line of work has been conducted with the dynamic model taken into account explicitly, while a very specific type of "string stability" is achieved for multiple autonomous vehicles.

In contrast to this, the approach suggested in this paper is platform-independent, proven successful, and general enough to support a number of different actual controllers. The idea that we capitalize on is that the tracking controllers can be designed independently of the coordination scheme, which provides us with additional control power.

Manuscript received April 20, 2000; revised August 3, 2001. This paper was recommended for publication by Associate Editor L. Kavraki and Editor V. Lumelsky upon evaluation of the reviewers' comments. The work of M. Egerstedt was supported in part by the Army Research Office under Grant DAAG 5597-1-0114, and in part by the Sweden–America Foundation 2000 Research Grant. The work of X. Hu was supported in part by the Swedish Foundation for Strategic Research through its Centre for Autonomous Systems at KTH, in part by TFR. This work was presented in part at ICRA, Seoul, Korea, May 2001.

M. Egerstedt is with the School of Electrical and Computer Engineering, Georgia Institute of Technology, Atlanta, GA 30332 USA (e-mail: magnus@ece.gatech.edu).

X. Hu is with the Division of Optimization and Systems Theory, Royal Institute of Technology, Stockholm, Sweden (e-mail: hu@math.kth.se).

Publisher Item Identifier S 1042-296X(01)10916-X.